Combining Atomistic Simulation and X-ray Diffraction for the Characterization of Nanostructures: A Case Study on Fivefold Twinned Nanowires

Florian Niekiel,[†] Erik Bitzek,[‡] and Erdmann Spiecker[†,*]

[†]Center for Nanoanalysis and Electron Microscopy (CENEM), Friedrich-Alexander-Universität Erlangen-Nürnberg, 91058 Erlangen, Germany and [‡]General Materials Properties, Friedrich-Alexander-Universität Erlangen-Nürnberg, 91058 Erlangen, Germany

ABSTRACT Recent progress in achieving high degrees of monodispersity in chemical synthesis of complex nanostructures creates the unique situation in which individual nanostructures become representative for the whole ensemble. Under these conditions, atomistic simulations can play a completely new role in interpreting structural data obtained from averaging techniques. We apply this approach to fivefold twinned Ag nanowires for which the existence of an ambient-stable tetragonal phase in the nanowire core has been recently proposed. Quantitative comparison of experimental X-ray diffraction data with atomistic calculations unequivocally shows that the diffractograms can be fully explained by the complex strain state and defect structure of fivefold twinned Ag nanowires with fcc crystal structure. In addition, our approach enables rapid and accurate determination of wire diameters by a modified Scherrer analysis which uses a database generated by atomistic simulations.

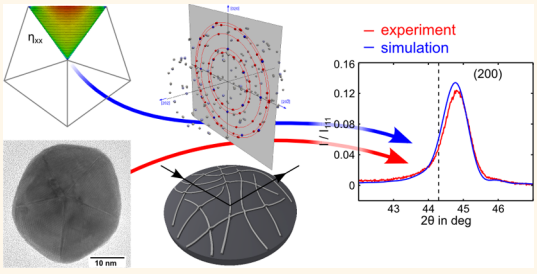

KEYWORDS: fivefold twinned nanowires · X-ray diffraction · atomistic simulation · disclination

The success of nanotechnology hinges on the controlled fabrication of millions to billions of identical nanostructures. This is because size, shape and composition critically influence the physical properties exploited in functional devices, like plasmonic resonances of metallic nanostructures[1,2] and band gaps of quantum dots.[3,4] New techniques to control the shape of increasingly more complex nanostructures are developed.[5,6] The need for identical nanostructures has spurred tremendous progress in achieving high degrees of monodispersity using concepts like templating,[7] self-limited growth,[8,9] surfactant molecules,[10,11] external stimuli,[12,13] or by applying advanced classification schemes.[14] Further optimization of synthesis routes requires quantitative characterization of large ensembles of nanostructures. A comprehensive characterization is furthermore important for the development of quantitative physical models and in identifying novel structure–property relationships.

Nanostructures are typically characterized individually using microscopic (*e.g.*, transmission electron microscopy (TEM)) techniques or as ensembles by spatially averaging (*e.g.*, X-ray diffraction (XRD)) methods. Currently, spatially averaging techniques are often used for quality control, whereas microscopic studies on individual nanostructures are more and more combined with atomistic modeling, which nowadays allows the material specific simulation of large and complex nanostructures. So far, the direct comparison of XRD and atomistic simulations has been limited to very small nanocrystals[15−17] or nanocrystalline materials.[18−22] Hardly any work exists that exploits the feasibility of atomistic simulations to quantitatively model XRD data of larger and more complex nanostructures. A different approach is to probe single isolated

* Address correspondence to Erdmann.Spiecker@ww.uni-erlangen.de.

Received for review November 16, 2013 and accepted January 13, 2014.

Published online January 13, 2014
10.1021/nn405941m

nanostructures in sophisticated X-ray diffraction setups at beamline facilities, *e.g.*, the study on the composition and strain of a Ag/Au core−shell nanowire using coherent X-ray diffraction.[23] However, the now achievable, unprecedented degrees of monodispersity open up new possibilities to use atomistic simulations for the quantitative evaluation of averaged data easily accessible from widely used laboratory equipment.

Wet-chemical or gas synthesis routes for the fabrication of nanostructures usually do not result in a well-defined crystallographic orientation on a substrate. Powder diffraction data obtained in Bragg−Brentano geometry are therefore frequently used for estimating nanoparticle size and internal strain based on concepts like the Scherrer formula or Williamson-Hall plots.[24,25] However, these concepts rely on approximations which are generally not applicable in the case of complex nanostructures.[26,27] For highly monodisperse nanoparticles with a distinct structure, a direct comparison with simulated diffraction data based on atomistic models is expected to be much more appropriate.

An example for such nanostructures are fivefold twinned Ag nanowires in which five twin boundaries intersect at the nanowire axis and, due to the closure error between the twin segments, create considerable internal strain, see Figure 1A,B. These nanowires are not only fascinating because of their unique structural properties,[28−31] but have recently attracted considerable interest due to their use in transparent electrodes[32−34] for organic solar cells.[35−37] Ag nanowire networks deposited by doctor blading or spray coating have already reached the low sheet resistance and high optical transmission of state-of-the-art sputtered ITO films and, moreover, show advantages with respect to their fabrication and mechanical properties making them particularly interesting for flexible electronics. The dimensions and the strain state of these nanowires have a large influence on their stability and mechanical integrity and play a key role for their performance in transparent electrodes.[38−40]

Recently, Sun *et al.*[41] used high-resolution X-ray diffraction to study the internal structure of fivefold twinned Ag nanowires. On the basis of the observation of peak splitting, which is not expected for the face-centered cubic (fcc) crystal structure of bulk silver, a novel body-centered tetragonal phase has been proposed. The authors conclude that the "fivefold twinning structure is key to the formation and stability of this tetragonal phase", which is stable "even at ambient conditions".[41] The new silver phase is supposed to be stabilized in the core of the nanowires. This claim is supported by the observation that galvanic removal of the core results in a gradual loss of peak splitting in in situ XRD experiments. However, no comparison of experimental X-ray diffractograms with calculated diffractograms based on an atomistic model has been done at any stage of the work.

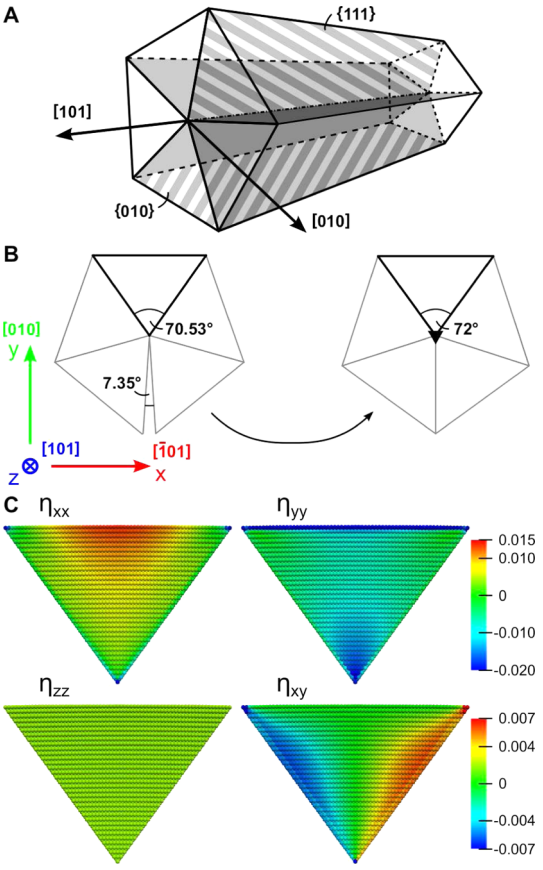

Figure 1. Structure of fivefold twinned nanowires: (A) crystallographic directions, (B) closure of the 7.35° gap by a positive partial wedge disclination, (C) atomic strain state in the simulated relaxed fivefold twinned Ag nanowire (d^* = 29 nm). The shown segment is in the same orientation like the one highlighted in (B). Introduction of coordiante system of crystal directions which is used throughout this work. The coordinate system refers to the segment shown with bold lines.

In the present work we use atomistic simulation based on semiempirical many body potentials in combination with XRD experiments to study the inner structure of monodisperse fivefold twinned Ag nanowires. Experimental X-ray diffractograms are measured in Bragg−Brentano geometry exploiting the texture effect of nanowires dispersed on a substrate. The size distribution and defect structure of the nanowires are independently evaluated by TEM. Molecular statics simulations are employed to produce equilibrium atomic configurations of the fivefold twinned nanowires, which in a second step are used to calculate X-ray diffractograms. For this, the well-known Debye formula is modified to account for texture. The complementary experimental and simulation approach allows us to confirm that fivefold twinning in combination with the naturally occurring disclination strain field accommodating for the 7.35° angular gap consistently describes the inner structure of the nanowires. There is no need to introduce an "ambient-stable tetragonal phase" as suggested by Sun *et al.*[41] Moreover, features

in the diffractogram sensitive to plastic strain relaxation are identified. Finally, a modified Scherrer analysis for quick and reliable determination of wire diameters is established which is very useful for practical applications. Our exemplary study shows the great potential of using atomistic simulations for quantitative evaluation of X-ray diffractograms of monodisperse nanostructures.

RESULTS AND DISCUSSION

To first illustrate the expected strain state of the fivefold twinned Ag nanowires, Figure 1C shows the strain distribution inside one segment of a representative nanowire (diameter $d^* = 29$ nm) calculated from molecular statics simulations as described in the Materials and Methods. The four different strain components, η_{xx}, η_{yy}, η_{zz} and η_{xy} are represented as color maps overlaid onto the atomic configuration, while η_{xz} and η_{yz} have been observed to be zero. To increase the wedge angle of a perfect fcc segment from 70.53° to 72°, the segment has to be strained in tension along the [$\bar{1}$01] direction and/or in compression along the [010] direction (using the coordinate system introduced in Figure 1). The tensile strain along [$\bar{1}$01] is reproduced in the atomistic calculations by the red and yellow color in the η_{xx} map. The strain is not uniform but is largely localized at the upper center part of the segment adjacent to the nanowire surface. Similarly, the compressive strain along [010] reproduced by the blue color in the η_{yy} map is not uniform. In this case, the strain is largest close to the center and at the very surface of the nanowire due to surface relaxation. The strain in the cross-sectional plane also introduces strain η_{zz} along the wire axis *via* transversal contraction. Due to the applied periodic boundary conditions, η_{zz} is uniform across the wire section. Finally, the shear strain η_{xy} is most pronounced along the twin boundaries. Regarding the size effect on the strain state of fivefold twinned Ag nanowires, the strain distribution has been found to be self-similar for the investigated sizes.

Figure 2 summarizes results of a microscopic evaluation of the real Ag nanowires selected for this study. First, Figure 2A shows a scanning electron microscopy (SEM) image of Ag nanowires dispersed on a silicon substrate, similar to the situation in the X-ray diffraction experiment. The preferential orientation of nanowires parallel to the substrate surface is clearly visible. Figure 2B shows a typical plan-view TEM image of nanowires dispersed on a C-foil. The variation of the contrast along the wire axis is due to slight bending of the wires giving rise to bend contour contrast. The ensemble of nanowires appears to be monodisperse. To evaluate the size distribution of the nanowires, the projected diameters d of 99 nanowires have been measured from plan-view TEM images at higher resolution. The corresponding diameter distribution is depicted in Figure 2C and is characterized by a mean diameter of 32.6 nm and a standard deviation of

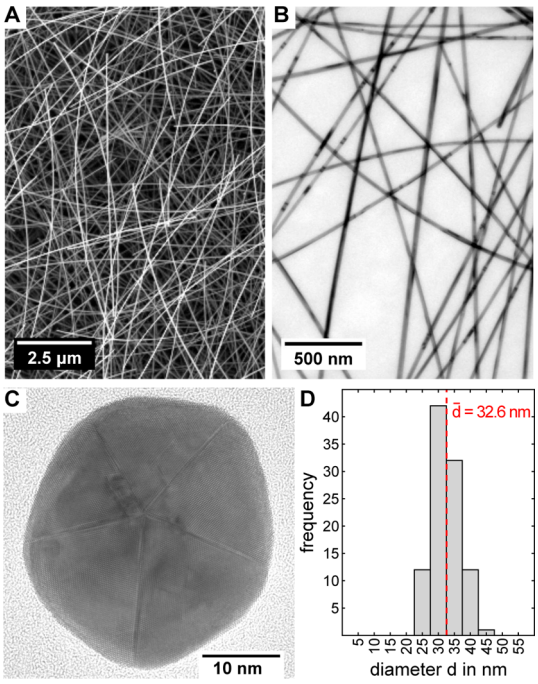

Figure 2. Microscopic evaluation of fivefold twinned Ag nanowires: (A) SEM image of nanowires dispersed on a silicon substrate, (B) CTEM plan-view image of nanowires dispersed onto C-foil, (C) HRTEM image of nanowire cross section prepared by shadow FIB (see Supporting Information for better resolution of HRTEM image), (D) distribution of projected diameters d of 99 nanowires measured from CTEM plan-view images.

4.2 nm. From the HRTEM image of a typical wire cross section shown in Figure 2D, the fivefold twinned structure is clearly visible. (The image is available in a better resolution in the Supporting Information.) The real wires slightly deviate from the ideal structure depicted in Figure 1A, which was used for the atomistic simulations in Figure 1C. The wire surface is slightly rounded, thus deviating from {100}. Moreover, the intersection line of the five twins is generally slightly displaced from the center of the wire. Finally, the real wires often contain some stacking faults inside the segments indicating that part of the internal strain is released by the glide of partial dislocations, which are incorporated in the twin planes.[42] In contrast to the rather uniform wire diameter, these features slightly deviate from wire to wire. Therefore, we consider the fully strained wire shown in Figure 1C to be the most reasonable model to start with. Of course, the above-mentioned deviations from ideal wire geometry and internal structure have to be taken into account when comparing experiments and simulations as will be shown for X-ray diffractograms.

Figure 3 illustrates the geometry of our XRD experiments in direct and reciprocal space. Due to Bragg–Brentano geometry, only lattice planes parallel to the substrate contribute to the measured diffractogram corresponding to scattering vectors $\vec{h}$ perpendicular to the substrate surface. Since the dispersed nanowires

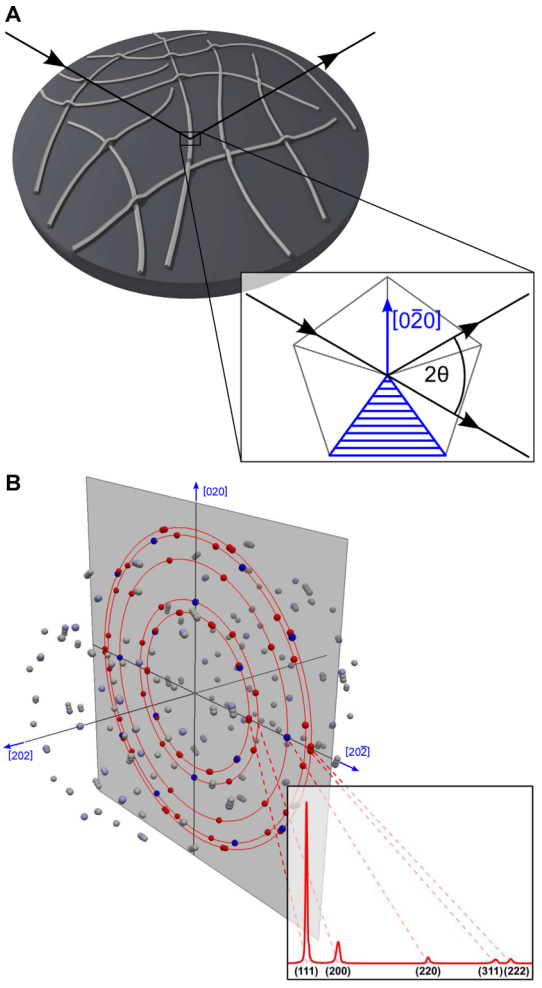

Figure 3. Schematic illustration of experimental setup exploiting the texture effect: (A) sketch of fivefold twinned nanowires dispersed on a substrate, inset exemplarily showing (020) planes of one segment being in condition for strong diffraction; (B) drawing of the reciprocal space of one fivefold twinned nanowire (only kinematically allowed reflections up to (222)); blue and bluish reflections correspond to one segment as highlighted in (A); plane illustrates circular averaging over red and blue reflections due to rotational degree of freedom of nanowires. The inset shows a possible XRD diffractogram.

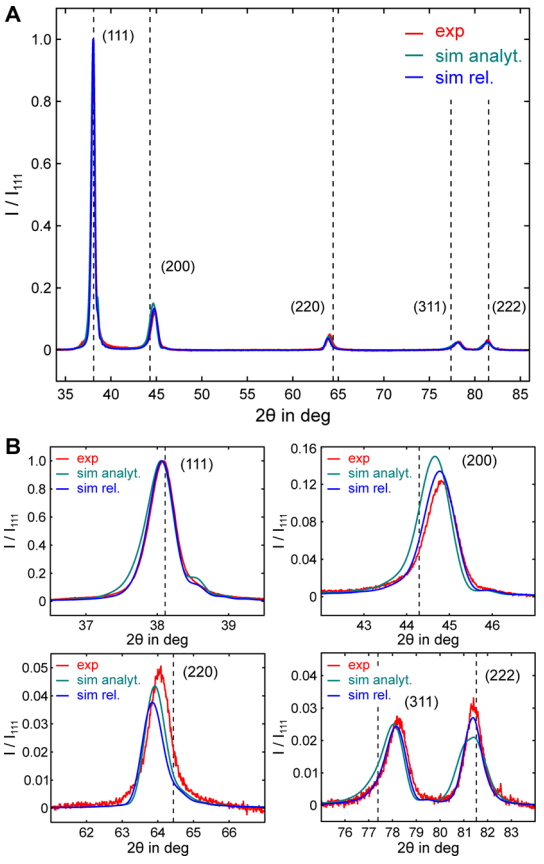

Figure 4. X-ray diffractograms of Ag nanowires: from experiment (red curve), calculated from simulation of relaxed fivefold twinned nanowire (d^* = 29 nm) (blue curve), calculated from unrelaxed fivefold twinned nanowire (d^* = 29 nm) with atoms displaced according to the analytical displacement field of a positive partial wedge disclination with ω = 7.35° (cyan curve) for a linear elastic isotropic material. Dashed lines indicate theoretically expected peak positions for perfect fcc Ag (a = 0.409 nm).

lie flat on the substrate, only lattice planes parallel to the wire axis are expected to contribute corresponding to scattering vectors in the cross-sectional plane of the wires. At intersection points, nanowires lie on top of each other thus deviating from the flat geometry. However, unless the local curvature is considerable, low-index diffraction vectors not contained in the wire cross section will hardly reach Bragg condition. Averaging over the whole sample, the signal can therefore be expected to be almost exclusively determined by scattering vectors perpendicular to the wire axis. This geometric texture effect allows us to probe selectively the cross-sectional size and strain state of the fivefold twinned nanowires. Assuming that the rotational orientation of the nanowires on the substrate is statistical, which is strongly supported by our results (see below), the diffraction intensity of many nanowires is determined by rotational averaging (or integration) in a plane perpendicular to the nanowire axis in reciprocal space, as sketched in Figure 3B.

The experimental diffractogram of dispersed Ag nanowires is depicted in Figure 4A (red curve). The individual diffraction peaks are shown enlarged in Figure 4B. The peak positions are considerably shifted with respect to the values expected for perfect fcc Ag (dashed vertical lines), which is a direct consequence of the lattice strain in the nanowires (*cf.* Figure 1C). In agreement with the tensile strain η_{xx} of the (220) lattice planes and the compressive strain η_{yy} of the (200) lattice planes, the corresponding peaks are shifted to smaller and larger 2θ-values, respectively. However, a more detailed analysis of the peak positions and peak breadths and their relationship to the nonuniform strain and finite size of the nanowires requires a detailed quantitative study based on the results of atomistic simulation.

To achieve this, X-ray diffractograms have been calculated from the relaxed atomistic configurations

using kinematic diffraction theory as described by the well-known Debye formula.[43] To account for the geometric texture discussed above, the spherical integration has to be replaced by a circular integration in the plane perpendicular to the wire axis in reciprocal space (*cf.* Figure 3B). A similar approach has been employed to enhance the interpretability of X-ray diffractograms of nanocrystalline materials.[18−22]The resulting diffraction intensity $I(h)$ of an atomistic configuration of N atoms of same kind with atomic scattering factor $f(h)$ is given by

$$I(h) \propto f(h)^2[N + \int_0^\infty p(r_{ij}^{cs})J_0(2\pi h r_{ij}^{cs})\, dr_{ij}^{cs}] \qquad (1)$$

with the pair distribution function $p(r_{ij}^{cs})$ of the configuration, r_{ij}^{cs} the projected distance of two atoms onto the cross-sectional plane and J_0 the zero order Bessel function of the first kind (see Supporting Information).

To be able to directly compare the calculated diffractograms to the experimentally observed, the calculated diffractograms have been modified by polarization factor, Lorentz factor, geometry factor and Debye−Waller factor. To account for the occurrence of Cu-Kα1 and -Kα2 radiation in the experiment, these have been superposed in the calculated diffractograms (for more details see Supporting Information). Finally, to study the effect of nanowire size on the diffraction profile and to find the "best fit" to the experimental measurement, X-ray diffractograms have been calculated for nanowires with different diameters ranging between 13 and 45 nm.

Figure 4 directly compares the experimental X-ray diffractogram discussed above (red curve) and the calculated X-ray diffractogram constituting the "best fit" (blue curve). The best fit was obtained by adjusting the nanowire size in the simulation until the breadth of the dominating (111) peak equals the experimental value, which resulted in a nanowire diamter of d^* = 29 nm. Almost identical diameters (±1.5 nm) are obtained when the breadths of the diffraction peaks (200) or (220) are used instead (see below). On the basis of the fact that the atomistic simulations are carried out with an idealized nanowire structure and that the wire diameter is the only parameter that has been adjusted, an excellent agreement between calculated and measured X-ray diffractograms is achieved. For the (111), (200), (311) and (222) diffraction peaks, the simulation nicely reproduces all the observed peak shifts as well as the peak breadths and peak heights (see Figure 4 and Table 1). Only the (220) peak is not perfectly reproduced showing significant differences in peak position and peak height. The main characteristics of the diffraction peaks for the Ag nanowires, *i.e.*, peak position and peak breadth (FWHM), are summarized for the experimental data and the shown "best fit" simulation in Table 1.

To show the applicability of disclination theory to the microstructure of fivefold twinned nanowires, one more X-ray diffractogram has been calculated. The analytical linear elastic solution for the displacement field of a $\omega = 7.35°$ positive partial wedge disclination in a cylindrical disk of isotropic material as described by De Wit[44] has been applied to an unrelaxed atomistic configuration with atoms positioned according to the perfect fcc lattice in the five nanowire segments. The calculated X-ray diffractogram, which has been added to Figure 4 (cyan curve), shows that already the analytical disclination strain field nicely accounts for the observed peak positions, peak heights and peak breadths of (111), (200), (311) and (222). The correspondence is however not as good as for the "best fit" obtained with atomistic simulation. This is expected since the analytical model is based on isotropic elasticity and does not include surface effects.

TABLE 1. Peak Positions and Peak Widths of X-ray Diffractograms of Fivefold Twinned Ag Nanowires from Experiment ($2\theta_{max,exp}$, $FWHM_{exp}$) and from Relaxed Simulation d^* = 29 nm ($2\theta_{max,sim}$, $FWHM_{sim}$); Theoretical Peak Positions ($2\theta_{theo}$) for a = 0.409 nm fcc Silver

peak	$2\theta_{theo}$/ (deg)	$2\theta_{max,exp}$/ (deg)	$FWHM_{exp}$/ (deg)	$2\theta_{max,sim}$/ (deg)	$FWHM_{sim}$/ (deg)
111	38.11	38.07	0.42	38.06	0.42
200	44.29	44.80	0.83	44.75	0.84
220	64.44	64.05	0.72	63.87	0.69
311	77.39	78.19	1.02	78.10	1.03
222	81.53	81.43	0.84	81.38	0.94

The nanowire diameter of d^* = 29 nm obtained by adjusting the calculated XRD diffractogram to the experimental one is only slightly smaller than the value of d = 32.6 nm derived from plan-view TEM images (*cf.* Figure 2). This further supports that the idealized nanowire structure used in the atomistic simulation is an appropriate model for the real nanowires. The slightly smaller diameter obtained with the "best fit" simulation indicates that one (or more) sources of peak broadening in the real nanowires are not correctly reflected in the model. (It has, however, to be noted that the definition of d^* as the diameter of a cylinder of equivalent cross-sectional area in the simulations differs from the observed projected diameter d in plan-view CTEM.) Most likely, peak broadening results from the presence of extended defects which partly release lattice strain, like partial dislocations in the twinning planes connected to stacking faults.[42] Strain releasing lattice defects could also explain why the (220) diffraction peak in the experimental X-ray diffractogram is shifted from the "best fit" simulation (blue) toward the expected peak position for a perfect fcc lattice (dashed line). Interestingly, the other two diffraction peaks sensitive to strain, (200) and (311), are nicely described by the "best fit" simulation and do not show corresponding shifts toward the perfect fcc peak position. This may be explained by the fact that dislocations

incorporated in the twin planes mainly release strain in the outer part of the nanowires. According to Figure 1C, the tensile strain η_{xx} parallel to [$\bar{2}$02] is strongest in this part of the nanowire and is thus expected to be most strongly affected. In contrast, the compressive strain η_{yy} parallel to [020] is concentrated in the center of the nanowire and is thus expected to be largely unaffected by the presence of dislocations in outer regions of the nanowire. This argumentation is further supported by the pronounced shift (in the expected direction) of the (220) peak in a diffractogram calculated for a nanowire with a single partial dislocation connected to a stacking fault (see Supporting Information).

How can we understand the discrepancy between our results and the recently reported findings by Sun *et al.* who investigated similar Ag nanowires and observed "noticeable peak splitting not expected for the fcc phase"?[41] (For the reader's convenience and the subsequent discussion, their peak profiles are reproduced in Figure 5A.) On the basis of these profiles and the gradual loss of peak splitting during transformation of the Ag nanowires into Ag−Au alloy nanotubes, they proposed the existence of a "novel ambient-stable tetragonal phase" of Ag in the core of the nanowires.[41] The apparent discrepancy can be easily resolved by taking into account the absence (or low degree) of texture in the diffraction experiments by Sun *et al.* In their diffraction studies the Ag nanowires were sandwiched between Kapton tapes and the X-ray diffractograms were taken in transmission mode. Even though it is unlikely that the orientation of the nanowires is completely random a pronounced texture has obviously not been established by this preparation. In fact, Sun *et al.* reported that the same peak splitting occurred for nanowires dispersed in solution.

In the following we show that our atomistic simulations can also explain the peak splittings in the experimental X-ray diffractograms by Sun *et al.* To account for a random orientation of the Ag nanowires in calculated X-ray diffractograms, the well-known Debye formula has to be used instead of eq 1. For a monatomic configuration of N atoms having atomic scattering factor $f(h)$, the intensity is proportional to

$$I(h) \propto f(h)^2 [N + \int_0^\infty p(r_{ij}) \mathrm{sinc}(\pi h r_{ij})\, \mathrm{d}r_{ij}] \qquad (2)$$

utilizing the pair distribution function $p(r_{ij})$, r_{ij} being the distance between atom i and j (see Supporting Information for more details). In contrast to eq 1, the Debye formula in eq 2 averages over all possible crystal orientations implying that there is no preferential orientation or texture effect.

Figure 5B shows the X-ray diffractogram of a relaxed fivefold twinned Ag nanowire (d^* = 45 nm) calculated with eq 2. To allow for a direct comparison with the peak positions in the experimental X-ray diffractogram

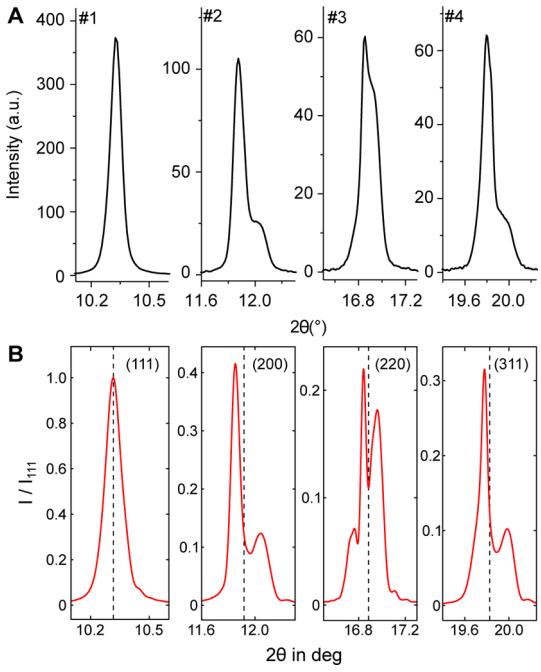

Figure 5. Comparison of (A) high-resolution X-ray diffractograms of Ag nanowires reported by Sun *et al.*[41] and (B) calculated from simulation of relaxed fivefold twinned nanowire (d^* = 45 nm) with a wavelength of 0.042460 nm. Dashed lines indicate theoretically expected peak positions for perfect fcc Ag (a = 0.409 nm).

by Sun *et al.* (Figure 5A), the same wavelength (λ = 0.042460 nm) was used in the calcuation. Before directly comparing the calculated diffractogram with the experimental one, the position, shape and splitting of the individual diffraction peaks revealed in the simulation are discussed with respect to the strain state of the fivefold twinned Ag nanowires (*cf.* Figure 1C).

The {200} peak is split into two peaks due to two different strain states for the ⟨200⟩ directions. Following the coordinate system from Figure 1, the [010] direction shows compressive strain (as already discussed), whereas the [100] and [001] directions show the same amount of tensile strain, as they lie between the tensilely strained [$\bar{1}$01] and [101] direction and are symmetric with respect to the strain state. This results into a peak splitting shifting the (020) peak to higher 2θ-values and the (200) and (002) peaks to smaller 2θ-values. As can be seen from Figure 5B, the peak intensities follow a 1:2 ratio with the (020) peak being broader than the (200) and (002) peak. This could easily be explained by a stronger distribution in the strain state along [010] than along [100] and [001] as the latter get contribution from the uniformly strained [101] direction. However, the dimensions of the scattering volume also change with the different orientations in the wire, which also has an influence on peak breadth.

The {220} peak is split into three distinct peaks corresponding to three unequivalent ⟨110⟩ directions in the symmetry of the strain state. The [$\bar{1}$01] direction

(lying in the cross section) shows a distribution of significant tensile strain (as discussed above), while the [101] direction representing the wire axis shows a uniform tensile strain of only about 0.2%. The other four independent ⟨110⟩ directions lie within the twin planes inclined to the wire axis and are mainly affected by the compressive strain state in [010] direction. These three different strain states can be assigned to the three distinct {220} peaks in the calculated X-ray diffractograms. The significantly tensilely strained [$\bar{1}$01] direction corresponds to the {220} peak at the lowest angle while the [101] direction with its uniform but small tensile strain corresponds to the peak in the middle, being only slightly shifted to lower angles from the perfect fcc position. The other ⟨110⟩ directions and their compressive strain state correspond to the {220} peak at the right having the largest overall intensity. As before, the comparison of the breadths of the peaks corresponding to the [$\bar{1}$01] and [101] directions could be explained by the effect of broadening due to strain state distribution *versus* uniform strain not considering the influence of different dimensions of the scattering volume with different orientations. Similar considerations can be made for the {111} and {311} peaks.

The direct comparison of panels A and B in Figure 5 shows that all the peak positions and peak splittings observed by Sun *et al.* are reproduced by our calculations based on atomistic simulations. The minor differences between the experimental and simulated X-ray diffractograms can be ascribed to several influences. On the one hand, the simulations have been executed for a nanowire of d^* = 45 nm diameter, the largest diameter considered in our simulations, whereas the experiments by Sun *et al.*[41] have been performed on nanowires with an average diameter of 85 nm. This leads to a larger broadening of the peaks in the simulated X-ray diffractogram in comparison to the experimental one (see also Figure 6 for an estimate on the effect of size on peak breadth). On the other hand, the distribution in diameters for the experimental nanowires leads to a peak broadening in respect to the simulation. The effects of temperature (Debye−Waller factor) and diffraction geometry (polarization, Lorentz and geometry factor) have not been taken into account in this simulation, which would lead to a dampening of the intensities with increasing angle. Moreover there might have been some texture effects in the experiments due to the huge aspect ratio of nanowires as well as inner defects of the nanowires differing from the perfect geometry in the simulations (see Supporting Information for the effect of defects on the peak profiles).

The fact that the data by Sun *et al.*[41] are overall well reproduced by our simulations again confirms that fivefold twinned Ag nanowires are well described by an fcc phase with a complex but continuous strain distribution resulting from the partial wedge disclination compensating for the angular gap in the fivefold twinned

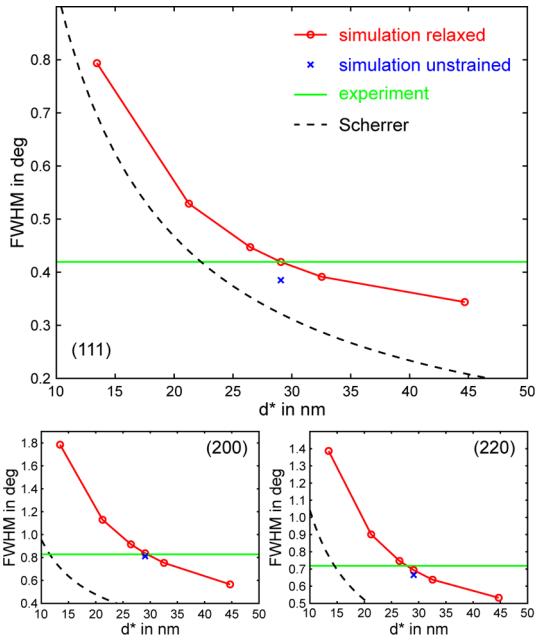

Figure 6. FWHM of the peaks observed in simulated X-ray diffractograms of relaxed fivefold twinned Ag nanowires in dependence of the diameter d^* (red) (lines are linear interpolations between data points); the FWHM observed in the experiment is drawn as green horizontal line, the FWHM of a simulated diffractogram of an unrelaxed fivefold twinned Ag nanowire with atoms in positions according to a perfect fcc lattice is drawn as blue cross, relationship according to Scherrer formula plotted as black dashed line.

microstructure. Obviously, there is no need to introduce a novel body-centered tetragonal phase of Ag for interpreting the XRD data.

A related discussion about a potential new phase has been held in the literature regarding multiply twinned decahedral and icosahedral nanoparticles.[45−51] Multiply twinned decahedral nanoparticles exhibit a similar microstructure as the fivefold twinned nanowires. The only difference is that they do not have a lateral extension (in the direction denoted [101] in Figure 1A) but are bordered by 10 {111} surface facets giving the nanoparticle the shape of a pentagonal bipyramid.[28] The microstructure of multiply twinned icosahedral nanoparticles consists of 20 subunits and is thus more complicated to compare to fivefold twinned nanowires. However, both types of multiply twinned nanoparticles are built from cubic crystals and exhibit the same closure error between the twin segments as the fivefold twinned nanowires. On the basis of conventional TEM studies, the group around Heinemann and Yacamán concluded that multiply twinned decahedral Au nanoparticles possess a body-centered orthorhombic crystal structure, as neither gaps nor an inhomogeneous lattice strain could be detected.[45−48] The group around Marks *et al.* performed a thorough theoretical analysis of the energetics of multiply twinned structures.[51] Their comparison of the models assuming a homogeneous body-centered orthorhombic crystal structure or an inhomogeneous strain state of the fcc structure due to a disclination clearly shows the

energetic favorability of an inhomogeneous strain state in the case of decahedral nanoparticles.[49] In a following experimental work, Marks showed the occurrence of inhomogeneous strain in multiply twinned nanoparticles revising the works by Heinemann, Yacamán and co-workers but underlines the issue of uniqueness of the interpretation.[50] In the meantime, the model of inhomogeneous strain appears to be generally accepted for the case of multiply twinned nanoparticles. The capabilities of modern equipment brought further insight, *e.g.*, the work by Johnson *et al.*[52] who mapped the strain distribution in decahedral Au nanoparticles using aberration-corrected high-resolution TEM. Very recently, Ophus *et al.*[53] investigated the strain distribution in multiply twinned decahedral RhPd nanoparticles using HRTEM focal series reconstructions in tandem with molecular statics simulations. Both studies clearly show the presence of inhomogeneous strain further supporting the model of disclination induced strain in multiply twinned nanoparticles with fcc crystal structure.

Our results for fivefold twinned Ag nanowires are in line with the described findings for nanoparticles. However, we emphasize that it is beyond the scope of the present study to show the uniqueness of the interpretation of the XRD data in terms of an atomistic model. Rather our approach starts with a reasonable atomistic model (strained fcc segments to fill the angular gap) which is structurally relaxed in atomistic simulations. From the resulting atomic configuration XRD data are calculated and compared with experimental XRD measurements. On the basis of our results we can firmly conclude that there is no need to introduce a novel phase of Ag since the normal fcc phase with its elastic properties can already nicely explain the experimental data. The fact that the atomic configuration resulting from the molecular statics simulations clearly exhibits an inhomogeneous strain state (Figure 1C) further supports the model of inhomogeneous strain as a homogeneous strain state (structurally equivalent to the proposed body-centered tetragonal phase) would have been a possible outcome of the simulations as well, especially as such a state has been used as initial configuration before relaxation.

Finally, in view of the application of XRD for quick characterization of nanowires, one may ask: What can be learned from $\theta - 2\theta$ diffractograms of monodisperse nanowire samples without carrying out extensive atomistic simulations, like in the present paper? Is it possible to directly deduce the diameter of the nanowires in a way similar to the Scherrer formula? Since the (111) peak is least affected by lattice strain, it is near at hand to use the breadth of this peak for evaluation of the nanowire diameter. With the use of the results of the atomistic simulation, the relationship between the nanowire diameter and the (111) peak breadth is depicted in the top part of Figure 6. The diagram furthermore shows the relationship given by the simple Scherrer formula (with geometric parameter $A = 1.0$), the peak breadth observed in the experiment (green horizontal line) and the simulation of a strain-free nanowire with atoms in positions according to a perfect fcc lattice of $d^* = 29$ nm diameter (blue cross). As expected, the Scherrer formula strongly underestimates the nanowire size since the coherent volume for diffraction is reduced by the fivefold twinning. More precisely, the coherent diffraction volume is reduced to the size of one segment of the fivefold twinned nanowire, with the only exception being the $\{111\}$ lattice planes, which are common to two adjacent nanowire segments. In addition, the maximum coherent volume may be further reduced by the presence of strain and defects. The lower part of Figure 6 shows the same plots for the (200) and (220) peaks, for which similar observations can be made.

With the use of a database of FWHM as function of nanowire diameter created from atomistic simulations (red curves in Figure 6), it is possible to directly evaluate the wire diameter for a monodisperse sample from the peak breadths in experimental X-ray diffractograms without having to worry about all the complicated effects of the particular microstructure. Such a modified Scherrer plot accounts for all the effects of size, strain and inner defects that are described in the atomistic simulation. The transfer of this approach to other nanostructures from the great diversity of today's nanotechnology is expected to be fruitful.

CONCLUSIONS

In summary, atomistic simulations based on semiempirical many body potentials have been combined with XRD experiments to gain insight into the inner structure of fivefold twinned Ag nanowires. The strong texture effect of nanowires dispersed on a flat substrate on XRD in Bragg–Brentano geometry has been exploited to selectively study size and strain in the cross-sectional plane of the nanowires. The direct comparison of experimental X-ray diffractograms with calculated diffractograms based on atomic coordinates from relaxed atomistic simulations or from the analytical displacement field of a partial wedge disclination convincingly demonstrates the applicability of disclination theory to describe the fivefold twinned microstructure. This leads to the conclusion that fivefold twinned Ag nanowires are well described by the normal fcc phase in the strain field of an $\omega = 7.35°$ positive partial wedge disclination. There is no need to introduce a "new" body-centered tetragonal phase of Ag (as suggested by Sun *et al.*[41]) to explain the experimental findings.

Our case study demonstrates the great potential of atomistic simulation to characterize nanostructured samples in tandem with XRD experiments if the samples show good monodispersity. The atomistic simulations can account for the intricate effects of size, strain fields

and defects and, therefore, allow a feasible characterization by XRD experiments. With a modified Scherrer analysis, the data provided in this work can be readily used to evaluate the diameters of fivefold twinned Ag nanowires from XRD in Bragg–Brentano geometry. We anticipate the use of atomistic simulation to become a key element in the quantitative XRD analysis of nanostructures and nanostructured materials.

MATERIALS AND METHODS

On the experimental side, fivefold twinned Ag nanowires similar to those used in transparent electrodes for organic solar cells[35−37] have been chosen for the study. For statistical evaluation of the wire diameters, the nanowires have been dispersed on a C-grid and studied by conventional TEM (CTEM). With the use of a shadow FIB (focused ion beam) technique,[54] individual Ag nanowires have been cut into cross sections thin enough for high-resolution TEM (HRTEM). CTEM and HRTEM investigations have been performed with a Philips CM300 microscope and an aberration-corrected FEI Titan^3 80-300 microscope, respectively. X-ray diffractograms have been acquired in Bragg–Brentano geometry using a Bruker D8 Advance diffractometer. To suppress diffraction contributions from the substrate, the nanowires have been dispersed on a vicinal (911) Si wafer. The $\theta - 2\theta$ diffractograms have been acquired for the range of $8° \leq 2\theta \leq 100°$ with a step size of 0.014°, and the background has been subtracted using a spline approximation. To ensure the machine calibration, a corundum standard calibration sample has been used.

On the simulation side, equilibrium configurations of fivefold twinned Ag nanowires at 0 K have been calculated by energy minimization using the fast inertial relaxation engine (FIRE)[55] to accommodate for the complex situation of fivefold twinning. The atomic interaction was modeled by the embedded atom method (EAM)[56,57] using the interaction potential for Ag by Williams *et al.*[58] The initial configurations of the perfectly pentagonal fivefold twinned nanowires with five {100} surfaces have been built placing atoms according to the lattice constant a = 0.409 nm given from the potential properties with a prestrain in tangential direction to compensate for the resulting misfit (compare Figure 1B). During optimization, the box length was allowed to change to reach an overall stress free state of the nanowire. Concerning the simulations, the diameter d^* is defined as the corresponding diameter of a cylinder of equal cross-sectional area. Periodic boundary conditions (PBC) have been applied along the nanowire axis to simulate infinitely long nanowires. The boxlengths were larger than 10 nm. The strain state in the relaxed configurations has been analyzed using the atomic strain tensor.[59] Visualization was done using ParaView.[60] The calculation of X-ray diffractograms based on atomistic configurations of the nanowires is described in the main text. To study the effect of size on the X-ray diffractograms and furthermore find the best fit to the experimental data, d has been varied between 13 and 45 nm in the atomistic simulations.

Conflict of Interest: The authors declare no competing financial interest.

Acknowledgment. This work has been financially supported by the DFG *via* the research training group 1896 "*In Situ* Microscopy with Electrons, X-rays and Scanning Probes" and the Cluster of Excellence EXC 315 "Engineering of Advanced Materials". The authors thank C.J. Brabec from the Institute of Materials for Electronics and Energy Technology at the University Erlangen-Nuremberg for providing the Ag nanowires used in this study. They further thank M. Klaumünzer from the Institute of Particle Technology for performing the $\theta - 2\theta$ XRD measurement and Christel Dieker for shadow-FIB preparation of the Ag nanowire cross section. Computational resources have been provided by RRZE HPC. F.N. thanks J. Li and his group (Massachusetts Institute of Technology, Cambridge) for inspiration and fruitful discussion.

Supporting Information Available: Additional information has been added to this work as noted throughout the text and includes calculation of XRD diffractograms from atomic configurations of nanowires, HRTEM of Ag nanowire cross section, effect of size on X-ray diffractograms, effect of defects on strain state and X-ray diffractograms. This material is available free of charge *via* the Internet at http://pubs.acs.org.

REFERENCES AND NOTES

1. Hao, E.; Bailey, R.; Schatz, G.; Hupp, J.; Li, S. Synthesis and Optical Properties of "Branched" Gold Nanocrystals. *Nano Lett.* **2004**, *4*, 32–330.
2. Rycenga, M.; Cobley, C.; Zeng, J.; Li, W.; Moran, C.; Zhang, Q.; Qin, D.; Xia, Y. Controlling the Synthesis and Assembly of Silver Nanostructures for Plasmonic Applications. *Chem. Rev.* **2011**, *111*, 3669–3712.
3. Smith, A.; Nie, S. Semiconductor Nanocrystals: Structure, Properties, and Band Gap Engineering. *Acc. Chem. Res.* **2010**, *43*, 190–200.
4. Regulacio, M.; Han, M.-Y. Composition-Tunable Alloyed Semiconductor Nanocrystals. *Acc. Chem. Res.* **2010**, *43*, 621–630.
5. Choi, C. L.; Alivisatos, A. P. From Artificial Atoms to Nanocrystal Molecules: Preparation and Properties of More Complex Nanostructures. *Annu. Rev. Phys. Chem.* **2010**, *61*, 369–389.
6. Xia, Y.; Xia, X.; Wang, Y.; Xie, S. Shape-Controlled Synthesis of Metal Nanocrystals. *MRS Bull.* **2013**, *38*, 335–344.
7. Hsueh, H.-Y.; Chen, H.-Y.; Hung, Y.-C.; Ling, Y.-C.; Gwo, S.; Ho, R.-M. Well-Defined Multibranched Gold with Surface Plasmon Resonance in Near-Infrared Region from Seeding Growth Approach Using Gyroid Block Copolymer Template. *Adv. Mater.* **2013**, *25*, 1780–1786.
8. Radmilovic, V.; Ophus, C.; Marquis, E.; Rossell, M.; Tolley, A.; Gautam, A.; Asta, M.; Dahmen, U. Highly Monodisperse Core-Shell Particles Created by Solid-State Reactions. *Nat. Mater.* **2011**, *10*, 710–715.
9. Bhattacharyya, S.; Bocker, C.; Heil, T.; Jinschek, J.; Höche, T.; Rüssel, C.; Kohl, H. Experimental Evidence of Self-Limited Growth of Nanocrystals in Glass. *Nano Lett.* **2009**, *9*, 2493–2496.
10. Zhang, Q.; Xie, J.; Yu, Y.; Lee, J. Y. Monodispersity Control in the Synthesis of Monometallic and Bimetallic Quasi-Spherical Gold and Silver Nanoparticles. *Nanoscale* **2010**, *2*, 1962–1975.
11. Ye, X.; Jin, L.; Caglayan, H.; Chen, J.; Xing, G.; Zheng, C.; Doan-Nguyen, V.; Kang, Y.; Engheta, N.; Kagan, C.; *et al.* Improved Size-Tunable Synthesis of Monodisperse Gold Nanorods through the Use of Aromatic Additives. *ACS Nano* **2012**, *6*, 2804–2817.
12. Wang, H.-Q.; Nann, T. Monodisperse Upconverting Nanocrystals by Microwave-Assisted Synthesis. *ACS Nano* **2009**, *3*, 3804–3808.
13. Zhang, J.; Langille, M.; Mirkin, C. Synthesis of Silver Nanorods by Low Energy Excitation of Spherical Plasmonic Seeds. *Nano Lett.* **2011**, *11*, 2495–2498.
14. Fanizza, E.; Depalo, N.; Clary, L.; Agostiano, A.; Striccoli, M.; Curri, M. A Combined Size Sorting Strategy for Monodisperse Plasmonic Nanostructures. *Nanoscale* **2013**, *5*, 3272–3282.
15. Zhang, H.; Gilbert, B.; Huang, F.; Banfield, J. F. Water-Driven Structure Transformation in Nanoparticles at Room Temperature. *Nature* **2003**, *424*, 1025–1029.
16. Gilbert, B.; Zhang, H.; Huang, F.; Banfield, J. F.; Ren, Y.; Haskel, D.; Lang, J. C.; Srajer, G.; Jürgensen, A.; Waychunas, G. A. Analysis and Simulation of the Structure of Nanoparticles that undergo a Surface-Driven Structural Transformation. *J. Chem. Phys.* **2004**, *120*, 11785.
17. Naicker, P. K.; Cummings, P. T.; Zhang, H.; Banfield, J. F. Characterization of Titanium Dioxide Nanoparticles Using Molecular Dynamics Simulations. *J. Phys. Chem. B* **2005**, *109*, 15243–15249.

18. Derlet, P. M.; Van Petegem, S.; Van Swygenhoven, H. Calculation of X-Ray Spectra for Nanocrystalline Materials. *Phys. Rev. B* **2005**, *71*, 024114.
19. Brandstetter, S.; Derlet, P. M.; Van Petegem, S.; Van Swygenhoven, H. Williamson-Hall anisotropy in nanocrystalline metals: X-ray diffraction experiments and atomistic simulations. *Acta Mater.* **2008**, *56*, 165–176.
20. Stukowski, A.; Markmann, J.; Weissmüller, J.; Albe, K. Atomistic Origin of Microstrain Broadening in Diffraction Data of Nanocrystalline Solids. *Acta Mater.* **2009**, *57*, 1648–1654.
21. Markmann, J.; Yamakov, V.; Weissmüller, J. Validating Grain Size Analysis from X-Ray Line Broadening: A Virtual Experiment. *Scr. Mater.* **2008**, *59*, 15–18.
22. Markmann, J.; Bachurin, D.; Shao, L.; Gumbsch, P.; Weissmüller, J. Microstrain in Nanocrystalline Solids under Load by Virtual Diffraction. *Europhys. Lett.* **2010**, *89*, 66002.
23. Haag, S.; Richard, M.-I.; Welzel, U.; Favre-Nicolin, V.; Balmes, O.; Richter, G.; Mittemeijer, E.; Thomas, O. Concentration and Strain Fields inside a Ag/Au Core-Shell Nanowire Studied by Coherent X-Ray Diffraction. *Nano Lett.* **2013**, *13*, 1883–1889.
24. Weibel, A.; Bouchet, R.; Boulc'h, F.; Knauth, P. The Big Problem of Small Particles: A Comparison of Methods for Determination of Particle Size in Nanocrystalline Anatase Powders. *Chem. Mater.* **2005**, *17*, 2378–2385.
25. Calvin, S.; Luo, S.; Caragianis-Broadbridge, C.; McGuinness, J.; Anderson, E.; Lehman, A.; Wee, K.; Morrison, S.; Kurihara, L. Comparison of Extended X-Ray Absorption Fine Structure and Scherrer Analysis of X-Ray Diffraction as Methods for Determining Mean Sizes of Polydisperse Nanoparticles. *Appl. Phys. Lett.* **2005**, *87*, 233102.
26. Scardi, P.; Leoni, M.; Delhez, R. Line Broadening Analysis Using Integral Breadth Methods: A Critical Review. *J. Appl. Crystallogr.* **2004**, *37*, 381–390.
27. Whitfield, P.; Mitchell, L. X-ray Diffraction Analysis of Nanoparticles: Recent Developments, Potential Problems and Some Solutions. *Int. J. Nanosci.* **2004**, *3*, 757–763.
28. Hofmeister, H. Forty Years Study of Fivefold Twinned Structures in Small Particles and Thin Films. *Cryst. Res. Technol.* **1998**, *33*, 3–25.
29. Chen, H.; Gao, Y.; Yu, H.; Zhang, H.; Liu, L.; Shi, Y.; Tian, H.; Xie, S.; Li, J. Structural Properties of Silver Nanorods with Fivefold Symmetry. *Micron* **2004**, *35*, 469–474.
30. Reyes-Gasga, J.; Elechiguerra, J.; Liu, C.; Camacho-Bragado, A.; Montejano-Carrizales, J.; Yacaman, M. On the Structure of Nanorods and Nanowires with Pentagonal Cross-Sections. *J. Cryst. Growth* **2006**, *286*, 162–172.
31. Damm, C.; Segets, D.; Yang, G.; Vieweg, B. F.; Spiecker, E.; Peukert, W. Shape Transformation Mechanism of Silver Nanorods in Aqueous Solution. *Small* **2011**, *7*, 147–156.
32. Hu, L.; Kim, H. S.; Lee, J.-Y.; Peumans, P.; Cui, Y. Scalable Coating and Properties of Transparent, Flexible, Silver Nanowire Electrodes. *ACS Nano* **2010**, *4*, 2955–2963.
33. Ellmer, K. Past Achievements and Future Challenges in the Development of Optically Transparent Electrodes. *Nat. Photonics* **2012**, *6*, 809–817.
34. Lee, J.; Lee, P.; Lee, H.; Hong, S.; Lee, I.; Yeo, J.; Lee, S.; Kim, T.-S.; Lee, D.; Ko, S. Room-Temperature Nanosoldering of a Very Long Metal Nanowire Network by Conducting-Polymer-Assisted Joining for a Flexible Touch-Panel Application. *Adv. Funct. Mater.* **2013**, *23*, 4171–4176.
35. Lee, J.-Y.; Connor, S. T.; Ciu, Y.; Peumans, P. Solution-Processed Metal Nanowire Mesh Transparent Electrodes. *Nano Lett.* **2008**, *8*, 689–692.
36. Krantz, J.; Richter, M.; Spallek, S.; Spiecker, E.; Brabec, C. J. Solution-Processed Metallic Nanowire Electrodes as Indium Tin Oxide Replacement for Thin-Film Solar Cells. *Adv. Funct. Mater.* **2011**, *21*, 4784–4787.
37. Guo, F.; Zhu, X.; Forberich, K.; Krantz, J.; Stubhan, T.; Salinas, M.; Halik, M.; Spallek, S.; Butz, B.; Spiecker, E.; *et al.* ITO-Free and Fully Solution-Processed Semitransparent Organic Solar Cells with High Fill Factors. *Adv. Energy Mater.* **2013**, *3*, 1062–1067.
38. Bergin, S. M.; Chen, Y.-H.; Rathmell, A. R.; Charbonneau, P.; Li, Z.-Y.; Wiley, B. J. The Effect of Nanowire Length and Diameter on the Properties of Transparent, Conducting Nanowire Films. *Nanoscale* **2012**, *4*, 1996–2004.
39. Sorel, S.; Lyons, P. E.; De, S.; Dickerson, J. C.; Coleman, J. N. The Dependence of the Optoelectrical Properties of Silver Nanowire Networks on Nanowire Length and Diameter. *Nanotechnology* **2012**, *23*, 185201.
40. Zhu, Y.; Qin, Q.; Xu, F.; Fan, F.; Ding, Y.; Zhang, T.; Wiley, B.; Wang, Z. Size Effects on Elasticity, Yielding, and Fracture of Silver Nanowires: *In Situ* Experiments. *Phys. Rev. B* **2012**, *85*, 045443.
41. Sun, Y.; Ren, Y.; Liu, Y.; Wen, J.; Okasinski, J. S.; Miller, D. J. Ambient-Stable Tetragonal Phase in Silver Nanostructures. *Nat. Commun.* **2012**, *3*, 971.
42. Monk, J.; Hoyt, J. J.; Farkas, D. Metastability of Multitwinned Ag Nanorods: Molecular Dynamics Study. *Phys. Rev. B* **2008**, *78*, 024112.
43. Debye, P. Zerstreuung von Röntgenstrahlen. *Ann. Phys.* **1915**, *351*, 809–823.
44. De Wit, R. Partial Disclinations. *J. Phys. C: Solid State Phys.* **1972**, *5*, 529–534.
45. Heinemann, K.; Yacamán, M. J.; Yang, C. Y.; Poppa, H. The Structure of Small, Vapor-Deposited Particles: I. Experimental Study of Single Crystals and Particles with Pentagonal Profiles. *J. Cryst. Growth* **1979**, *47*, 177–186.
46. Yacamán, M. J.; Heinemann, K.; Yang, C. Y.; Poppa, H. The Structure of Small, Vapor-Deposited Particles: II. Experimental Study of Particles with Hexagonal Profile. *J. Cryst. Growth* **1979**, *47*, 187–195.
47. Yang, C. Y. Crystallography of Decahedral and Icosahedral Particles: I. Geometry of Twinning. *J. Cryst. Growth* **1979**, *47*, 274–282.
48. Yang, C. Y.; Yacamán, M. J.; Heinemann, K. Crystallography of Decahedral and Icosahedral Particles: II. High Symmetry Orientations. *J. Cryst. Growth* **1979**, *47*, 283–290.
49. Howie, A.; Marks, L. D. Elastic Strains and the Energy Balance for Multiply Twinned Particles. *Philos. Mag. A* **1984**, *49*, 95–109.
50. Marks, L. D. Inhomogeneous Strains in Small Particles. *Surf. Sci.* **1985**, *150*, 302–318.
51. Ajayan, P. M.; Marks, L. D. Phase Instabilities in Small Particles. *Phase Transitions* **1990**, *24*−*26*, 229–258.
52. Johnson, C. L.; Snoeck, E.; Ezcurdia, M.; Rodríguez-González, B.; Pastoriza-Santos, I.; Liz-Marzán, L. M.; Hytch, M. J. Effects of Elastic Anisotropy on Strain Distributions in Decahedral Gold Nanoparticles. *Nat. Mater.* **2007**, *7*, 120–124.
53. Ophus, C.; Corthey, G.; Ercius, P.; Linck, M.; Radmilovic, V.; Salvarezza, R. C.; Dahmen, U. Modeling and Measuring the Strain State of Decahedral Nanoparticles *Proceedings European Micrososcopy Congress, 15th*, Manchester Central, U.K., September 16−21, **2012**.
54. Vieweg, B. F.; Butz, B.; Peukert, W.; Klupp Taylor, R. N.; Spiecker, E. TEM Preparation Method for Site- and Orientation-Specific Sectioning of Individual Anisotropic Nanoparticles Based on Shadow-FIB Geometry. *Ultramicroscopy* **2012**, *113*, 165–170.
55. Bitzek, E.; Koskinen, P.; Gähler, F.; Moseler, M.; Gumbsch, P. Structural Relaxation Made Simple. *Phys. Rev. Lett.* **2006**, *997*, 170201.
56. Daw, M. S.; Baskes, M. I. Embedded-Atom Method: Derivation and Application to Impurities, Surfaces, and other Defects in Metals. *Phys. Rev. B* **1984**, *29*, 6443–6453.
57. Daw, M. S.; Foiles, S. M.; Baskes, M. I. The Embedded-Atom Method: A Review of Theory and Applications. *Mater. Sci. Rep.* **1993**, *9*, 251–310.
58. Williams, P. L.; Mishin, Y.; Hamilton, J. C. An Embedded-Atom Potential for the Cu-Ag System. *Modell. Simul. Mater. Sci. Eng.* **2006**, *14*, 817–833.
59. Shimizu, F.; Ogata, S.; Li, J. Theory of Shear Banding in Metallic Glasses and Molecular Dynamics Calculations. *Mater. Trans.* **2007**, *48*, 2923–2927.
60. Kitware, Inc., ParaView: Parallel Visualization Applications. 2012; http://www.paraview.org/.